Article

Photo-expansion microscopy enables super-resolution imaging of cells embedded in 3D hydrogels

Kemal Arda Günay[1], Tze-Ling Chang[1], Nathaniel P. Skillin [1], Varsha V. Rao[1], Laura J. Macdougall[1], Alicia A. Cutler [2], Jason S. Silver[1,2], Tobin E. Brown[1], Chi Zhang[3,4,5], Chih-Chieh (Jay) Yu[3,4,5], Bradley B. Olwin [2], Edward S. Boyden[3,4,5] & Kristi S. Anseth [1] ✉

Hydrogels are extensively used as tunable, biomimetic three-dimensional cell culture matrices, but optically deep, high-resolution images are often difficult to obtain, limiting nanoscale quantification of cell–matrix interactions and outside-in signalling. Here we present photopolymerized hydrogels for expansion microscopy that enable optical clearance and tunable ×4.6–6.7 homogeneous expansion of not only monolayer cell cultures and tissue sections, but cells embedded within hydrogels. The photopolymerized hydrogels for expansion microscopy formulation relies on a rapid photoinitiated thiol/acrylate mixed-mode polymerization that is not inhibited by oxygen and decouples monomer diffusion from polymerization, which is particularly beneficial when expanding cells embedded within hydrogels. Using this technology, we visualize human mesenchymal stem cells and their interactions with nascently deposited proteins at <120 nm resolution when cultured in proteolytically degradable synthetic polyethylene glycol hydrogels. Results support the notion that focal adhesion maturation requires cellular fibronectin deposition; nuclear deformation precedes cellular spreading; and human mesenchymal stem cells display cell-surface metalloproteinases for matrix remodelling.

Expansion microscopy (ExM) is a technique based on isotropic enlargement of fixed biological specimens by the in situ polymerization of swellable, polyelectrolyte hydrogels[1]. Depending on the method and the hydrogel chemistry, ExM can provide ~4–20 times the linear expansion of the original sample[1–4], enabling the super-resolution imaging of cellular features using conventional confocal microscopy. Beyond the imaging of cells, ExM clears the sample, which is advantageous for the imaging of more complex, three-dimensional (3D) tissue samples[5]. ExM techniques have been used for the pathological screening of histological sections[5], interrogation of 3D tissue samples with single cell/molecule precision[6] and determination of subcellular RNA localization[7].

To date, the hydrogels used in ExM have been primarily synthesized by a chain polymerization of acrylate/acrylamide-based monomers using redox initiators[1,4]. However, this strategy often leads to longer sample preparation times and requires an inert atmosphere to mitigate oxygen inhibition[4], especially for thin samples. The reaction proceeds spontaneously, limiting temporal control and requiring

[1]Department of Chemical and Biological Engineering and the BioFrontiers Institute, University of Colorado, Boulder, CO, USA. [2]Department of Molecular, Cellular and Developmental Biology, University of Colorado, Boulder, CO, USA. [3]McGovern Institute, MIT, Cambridge, MA, USA. [4]HHMI, Cambridge, MA, USA. [5]Departments of Brain and Cognitive Sciences, Media Arts and Sciences, and Biological Engineering, MIT, Cambridge, MA, USA. ✉e-mail: Kristi.anseth@colorado.edu

careful experimental design to avoid premature gelation during permeation[8]. Moreover, while chain growth polymerizations are versatile, nanoscale non-idealities occur and can increase the spatial errors of fluorophore locations upon expansion[9]. Chain-polymerized hydrogels also have inferior mechanical properties compared to step-growth networks[10], which can complicate sample handling post expansion. Based on this premise, we sought to design complementary materials and methods for ExM that would decrease processing times, lead to robust materials and allow for uniform expansion of samples, even those with cells embedded in 3D microenvironments.

We developed formulations that allow a photoinitiated polymerization of hydrogels for expansion microscopy (PhotoExM). Photoinitiated polymerizations can be advantageous for ExM applications, as monomer diffusion into the biological sample (that is, mass transfer) is decoupled from the reaction kinetics for the hydrogel formation. The PhotoExM hydrogels reported herein were prepared by a mixed-mode thiol acrylate photopolymerization[11], which is oxygen insensitive[12], proceeds rapidly (time, $t = 70$ s) and enables benchtop fabrication. This fast and versatile method allows up to a ×6.7 uniform expansion of antibody-labelled biological samples, and the amount of expansion can be tuned by light exposure and the concentration of the crosslinker in the monomer formulation.

Beyond the two-dimensional (2D) cell culture and analysis of tissue sections, we further demonstrate that the PhotoExM method allows super-resolution imaging of cells embedded within hydrogel matrices. Synthetic hydrogels are extensively used for tissue engineering and regenerative medicine as in vivo cell delivery vehicles to promote tissue regeneration[13], as well as in vitro 3D culture models to study cell–matrix interactions and outside-in signalling[14,15]. However, imaging through 3D cell-laden materials poses similar challenges to those of tissues, such as light scattering and attenuation, which limit resolution and depth. To address these specific challenges, we developed a new PhotoExM-based technique that optically clears and expands biological samples, including cell-laden matrices. The method uses a gel-to-gel transfer (GtG) technique and allowed us to resolve nanoscale features of individual cells embedded within hydrogels, along with interactions with nascently deposited extracellular matrix (ECM) molecules in their pericellular microenvironment.

Design and characterization of PhotoExM hydrogels

PhotoExM hydrogels were prepared via photoinitiated mixed-mode thiol/acrylate polymerization, which is described in Supplementary Fig. 1 (refs. 11,16). Network growth in this mixed-mode reaction proceeds via simultaneous chain growth copolymerization of acrylamide, sodium acrylate (16 wt%) and polyethylene glycol (PEG)–diacrylamide crosslinker (PEGdiAcM; $M_n = 600$ g mol^{-1}), as well as step-growth polymerization through a chain transfer reaction between the multi-arm PEG-SH and propagating chain growth radicals (Fig. 1a). The mixed-mode reaction mechanism of the PhotoExM hydrogel formulations homogenizes the spatial position of the network crosslinking

points compared to pure chain growth networks (Fig. 1a)[10,17,18], which may decrease the spatial error of fluorophore positions post expansion. Although we did not perform a head-to-head comparison of PhotoExM to chain growth ExM networks, it was recently shown that a pure step-growth ExM network exhibited marked enhancements in expansion isotropy[9,19]. PhotoExM also results in gels with a higher elastic modulus and therefore greater resistance to deformation during handling compared to the original ExM chemistry (Supplementary Fig. 2). Furthermore, the shear modulus of the PhotoExM hydrogels prepared with 6 wt%, 8-arm, 10 kDa PEG-SH were substantially higher than hydrogels polymerized using 6 wt%, 4-arm, 5 kDa PEG-SH at identical PEGdiAcM wt%, as measured by rheology (Fig. 1b). This increase was attributed to the increased step-growth character of the 8-arm, 10 kDa PEG-SH-containing PhotoExM hydrogels despite identical thiol concentrations in both networks. Of further note, the increased step-growth character introduced by incorporating the 8-arm PEG-SH into the network decreases the crosslinker (PEGdiAcM) content required for hydrogel formation (Fig. 1b). Since the equilibrium swelling ratio of the hydrogel scales with the network crosslinking density to the approximately −3/5 power (as predicted via Flory–Rehner theory)[20], the decreased PEGdiAcM concentration enabled up to ×6.7 linear expansion of the PhotoExM hydrogels incorporating 8-arm, 10 kDa PEG-SH, which can be easily tuned by modifying the PEGdiAcM wt% (Fig. 1c). The hydrogels before and after expansion are shown in Fig. 1d.

Apart from greater crosslinking, shear moduli and tailorable expansion factors, photoinitiation of the formulations decouples monomer diffusion from gel formation, which is advantageous for the preparation, expansion and imaging of cell-laden 3D hydrogels. A schematic illustration of the PhotoExM process is summarized in Fig. 1e. Briefly, fixed and immunolabelled samples are first reacted with a heterobifunctional linker, 6-((acryloyl)amino)hexanoic acid succinimidyl ester (acryloyl-X), to introduce a polymerizable acrylamide group to the samples[3]. Next, PhotoExM formulations are premixed in phosphate-buffered saline (PBS) containing 2 M NaCl (and remain unreactive in the absence of light irradiation) and diffused into the biological sample of interest. The PhotoExM process uses a water soluble photoinitiator, lithium phenyl-2,4,6-trimethylbenzoylphosphinate (LAP), which generates radicals upon exposure to 365–405 nm light[21]. Relatively low light intensities ($I = 4.5$ mW cm^{-2}) are sufficient to polymerize the PhotoExM hydrogels, and gel formation reached >90% conversion within 70 s as measured by in situ photo-rheology (Fig. 1f). This rapid network evolution is a result of a single radical capable of propagating through multiple polymer chains via chain transfer reactions between propagating acrylate–acrylamide chain end radicals and thiol groups (Supplementary Fig. 1). This mechanism also recycles oxygen radicals[12], rendering the polymerization insensitive to ambient oxygen, which circumvents depth-dependent inhomogeneities that can arise from oxygen inhibition and eliminates inhibition at the surface, which can also be critical when expanding thin samples. Of further note, the irradiation wavelength (λ, 365 nm) is below the absorption range of most fluorophores used in immunolabelling,

Fig. 1 | PhotoExM process and formulations. a, Schematic representation of the network structure that results from chain and mixed-mode polymerizations: while stochastic organization of the crosslinking points can cause network heterogeneities, resulting in brittle hydrogels, mixed-mode polymerization homogenizes the spatial position of crosslinking points (green dots), improving the mechanical properties. Inset contains the PhotoExM formulation. Photoinitiated radicals propagate through the electrolyte (NaAc) and AcM monomers, and crosslinking occurs when PEGdiAcM is incorporated during chain growth, but the multi-arm PEG-SH acts as a chain transfer agent and introduces step-growth behaviour, and alters the network structure (yellow dots). **b**, Storage modulus (G') of PhotoExM formulations as a function of PEGdiAcM weight percent after 70 s of polymerization as measured by rheology. $N = 3$ hydrogels; data are presented as mean ± s.d. **c**, Size expansion factor

of PhotoExM formulations as a function of the PEGdiAcM weight percent. $N = 3$ hydrogels; data are presented as mean ± s.d. **d**, Representative images of PhotoExM hydrogels pre- and post expansion. Post-expansion hydrogel experiences a small amount of syneresis (~4%) between the time it was removed from H$_2$O and the image capture. **e**, Schematic illustration of the PhotoExM process. Fixed, immunolabelled and anchored samples were permeated with the PhotoExM formulation, which is photopolymerized for 70 s ($\lambda = 365$ nm, $I = 4.5$ mW cm^{-2}) using the photoinitiator LAP (0.2 wt%). Samples were digested with a Proteinase K-containing buffer and repeated H$_2$O washes (20 min each) yielded expanded biological samples. **f**, PhotoExM hydrogel evolution as a function of irradiation time ($I = 4.5$ mW cm^{-2}) using different crosslinker wt% as measured by rheology in the presence of 8-arm, 10 kDa PEG-SH (6 wt%). Displayed curves are the average of three independent measurements.

rendering PhotoExM compatible with many commercially available fluorophores (for example, Alexa Fluor 488; Supplementary Fig. 3). Following PhotoExM hydrogel formation, sample digestion is achieved by exposing the sample to a buffer containing Proteinase K, and subsequent hydrogel swelling by consecutive H$_2$O washes using established protocols enable hydrogel expansion[1]. With the current monomer
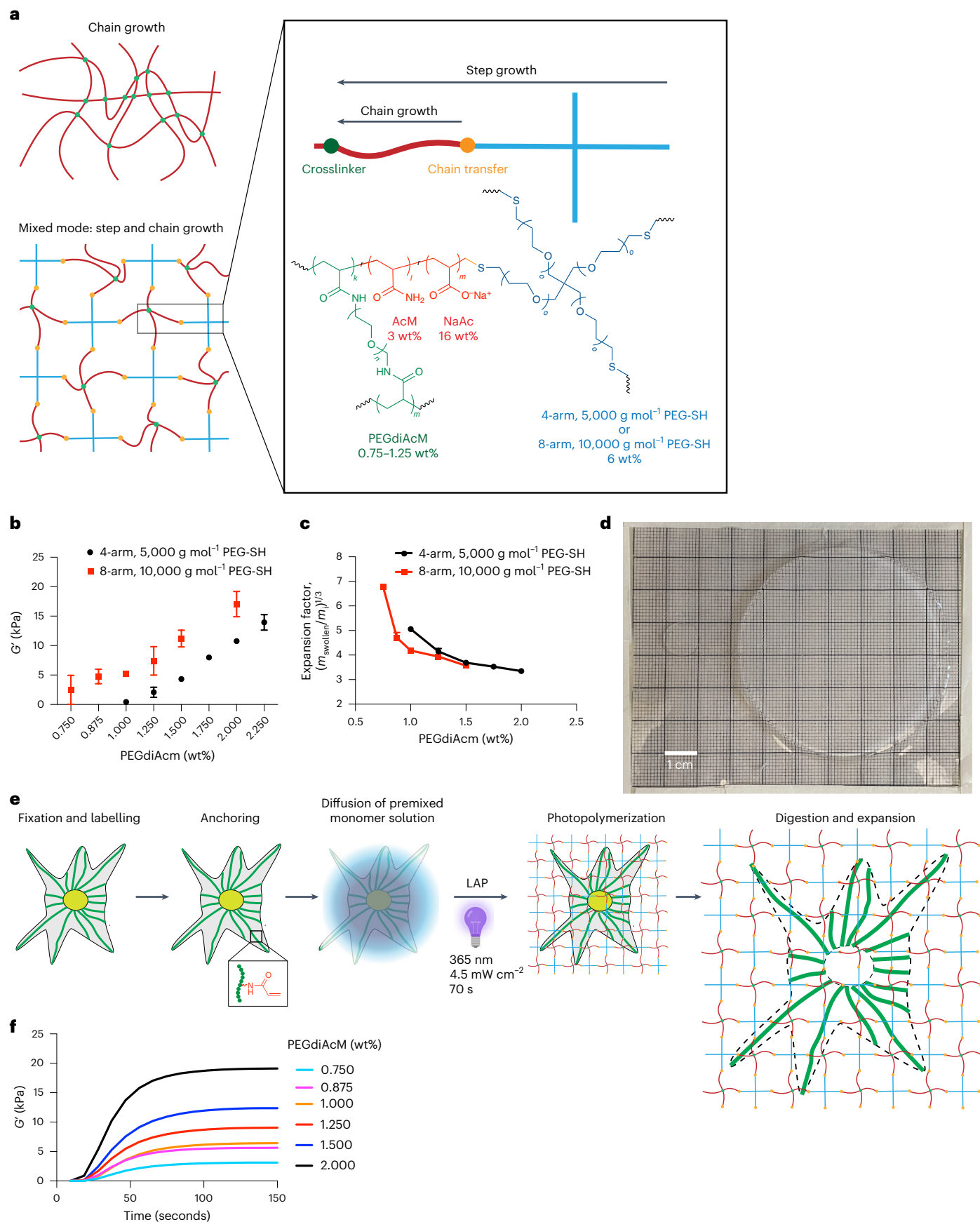
system, we show that biological samples can be magnified between ×4.6–6.7 of their original size and imaged with nanoscale resolution using standard fluorescence microscopes.

Validation and resolution of the PhotoExM method

To quantify the fidelity and homogeneity of the PhotoExM hydrogels, muscle myoblast cells (C2C12 cells) were cultured on coverslips, fixed and immunolabelled for α-tubulin. Identical areas were imaged before and after approximately ×4.6 sample expansion (Fig. 2a). The images were matched via a non-rigid registration process (Supplementary Fig. 4a)[1], allowing the calculation of the root mean square (r.m.s.) error of the sample features as a function of average measurement length (Fig. 2b). Over 20 μm, the average r.m.s. error was 2.8%, which is comparable to prior ExM methods but allows faster polymerization kinetics (70 s versus 90 min)[1,3]. However, measurement errors can further arise from the batch-to-batch variability of the hydrogel expansion factor; this was found to be ~2.1% (Fig. 2c), resulting in a cumulative error of 3.5% for the PhotoExM process.

We next assessed the resolution improvement achieved by PhotoExM by quantifying the full-width at half-maximum (FWHM) of microtubules before and after ×4.6–6.7 expansion (Fig. 2d). The measured microtubule diameter was 331 ± 32 nm prior to expansion, and it decreased to 90 ± 8 nm following the ×4.6 expansion, and 69 ± 7 nm after the ×6.7 expansion (Fig. 2e and Supplementary Fig. 4b). The latter was comparable to the measured diameters (d) of microtubules immunolabelled with primary and secondary antibodies ($d \approx 60–65$ nm)[4,22], demonstrating the super-resolution imaging capabilities of PhotoExM. We note that the resolution did not scale directly with the sample expansion factor, since labelled microtubules no longer act as point sources post expansion ($d \approx 276$ and 402 nm for ×4.6 and ×6.7 expansions, respectively, in non-scaled units). These values are comparable to the Abbe limit for the microscope's optical configuration (at numerical aperture (NA) = 1.0 and $\lambda = 488$ nm, the Abbe limit is 298 nm). As a result, while the theoretical resolution of an ideal point source is 44 nm with PhotoExM using this optical configuration, the effective optical resolution as measured by microtubules was 69 ± 7 nm.

Next, we used PhotoExM to visualize muscle tissue sections. Thick, longitudinal tibialis anterior muscle sections were isolated from six-month-old male mice, fixed and immunolabelled with α-actinin to visualize sarcomeres in the myofibres (Fig. 2f). Imaging of sarcomeres before and after ×4.6 expansion in different muscle sections enabled quantification of the expansion isotropy within tissue samples. The average distance between sarcomeres was 1.43 ± 0.19 and 6.35 ± 0.81 μm before and after ×4.6 expansion (in non-scaled units), respectively (Fig. 2g), where the variation in sarcomere length arises from different degree of muscle contraction[23]. The ratio between the average sarcomere length was 4.44, corresponding to an error of 3.0%, which is within the 3.5% error margin of the PhotoExM process (×4.6 expansion). Furthermore, PhotoExM was used to reveal the subcellular architecture of muscle stem cells (Pax7) on isolated myofibres and the myofibre–ECM interface (dystrophin), as well as the surrounding ECM (laminin) around the muscle stem cells (Supplementary Fig. 5), which are otherwise difficult to visualize due to the minimal cytoplasmic area and small size (~10 μm) of the muscle stem cells[24].

Nanoscale imaging in 3D hydrogels by GtG transfer

Synthetic hydrogels are extensively used as in vivo delivery systems to promote tissue regeneration and as 3D models to study disease and development in vitro[14]. While the 3D microenvironment can better recapitulate a cell's in vivo niche, analysis and imaging of cells with high resolution is more challenging. These complications arise not only because of the limited penetration depth of super-resolution microscopes, but also because of the light absorption and scattering

of cell-laden matrices. Collectively, this can limit the ability for the nanoscale imaging and interpretation of cell–matrix interactions and cellular processes. To address some of these challenges, we tailored the digestion step of PhotoExM to degrade the biological samples in parallel with the slightly opaque cell-laden hydrogel matrix, resulting in an optically clear gel that was subsequently expanded prior to imaging. This strategy, which we refer to as GtG, relies on the ability to decouple the diffusion of the PhotoExM components into the 3D hydrogel from the on-demand photopolymerization of the gel, which temporarily yields an interpenetrating network (Fig. 3a). The time required for uniform diffusion of PhotoExM components was estimated using the established mass transfer for diffusion as a function of molecular size and the crosslinking density of the hydrogel network (Methods, equation (6)). The GtG method was designed to be compatible with degradable 3D hydrogel cultures (that is, enzymatic, hydrolytic and photolytic), and the system can be degraded either simultaneously or sequentially during the digestion step, depending on the degradation mode (Fig. 3a)[25].

Using our newly developed GtG method, we first visualized human mesenchymal stem cells (hMSCs) and their interactions with nascently deposited ECM molecules. The hMSCs are highly secretory cells, which can lead to a feedback mechanism that dictates function, fate and mechanosensing[26,27]. However, less is known about how hMSCs interact with the pericellular deposited matrix and which mechanisms regulate those interactions. To investigate this more closely, we used our GtG PhotoExM method to image hMSCs encapsulated in matrix metalloproteinase (MMP)-degradable PEG-based hydrogels prepared by a strain-promoted azide/alkyne cycloaddition (SPAAC) reaction (Fig. 3b)[28]. A diazide-functionalized MMP-degradable crosslinker N_3-GVPMS↑MRGGK(N_3)G-N_3 was incorporated into the gel, which can be degraded by hMSCs or by exogenous delivery of Proteinase K. In addition, 1 mM of an azide-functionalized fibronectin-mimetic sequence N_3-KRGDS was incorporated to promote hMSC integrin binding and matrix adhesion. SPAAC hydrogels had a Young's modulus of $E' = 7.0 \pm 0.4$ kPa (Supplementary Fig. 6c). The hMSCs were encapsulated in the degradable SPAAC hydrogels at a density of 5×10^5 cells ml^{-1} under physiological conditions that preserved high viability (>92%; Supplementary Fig. 6a,b). The hMSC-laden hydrogels were fixed one, three and seven days post encapsulation and immunolabelled for fibronectin, collagen I and laminin (pan) to reveal variations in the ECM matrix composition and distribution. Samples were also immunolabelled for paxillin and integrin β1 to determine the matrix adhesion sites interacting with the newly deposited ECM. Then, samples were anchored with 0.1 mg ml^{-1} acryloyl-X treatment for 6 h, and permeated with the PhotoExM formulation two times for 30 min each at room temperature, which was longer than the calculated characteristic diffusion time of the PhotoExM formulation into the SPAAC hydrogel ($t \approx 5$ min; Methods, equation (6)). Photopolymerization for 70 s ($\lambda = 365$ nm, $I_o = 4.5$ mW cm^{-2}) yielded an interpenetrating network composed of SPAAC and PhotoExM hydrogels, and then SPAAC hydrogels and the embedded hMSCs were digested overnight at 37 °C and subsequently expanded with repeated H_2O washes. For these SPAAC hydrogels, we found the overall expansion factor to be approximately ×3.2 as a result of SPAAC hydrogel shrinkage during diffusion of the PhotoExM formulation (Supplementary Fig. 6d). Thus, the theoretical lateral resolution achieved in these experiments were ~113 nm in this optical configuration ($\lambda = 594$ nm, pinhole = 1 a.u., NA = 1.0). This substantial resolution improvement was evident when a head-to-head visualization of pre- and post-expansion images of hMSCs immunolabelled with fibronectin and paxillin and stained with 4′,6-diamidino-2-phenylindole (DAPI) were carried out one day post encapsulation (Supplementary Fig. 7).

Figure 3c shows representative 3D segmented images of hMSCs immunolabelled for fibronectin and paxillin following GtG. At day 1, hMSCs preserved their rounded morphology, yet substantial amounts of fibronectin were deposited, albeit with large cell-to-cell variability (105 ± 119 μm^3; Fig. 3c,d). After three days of culture, hMSCs remained
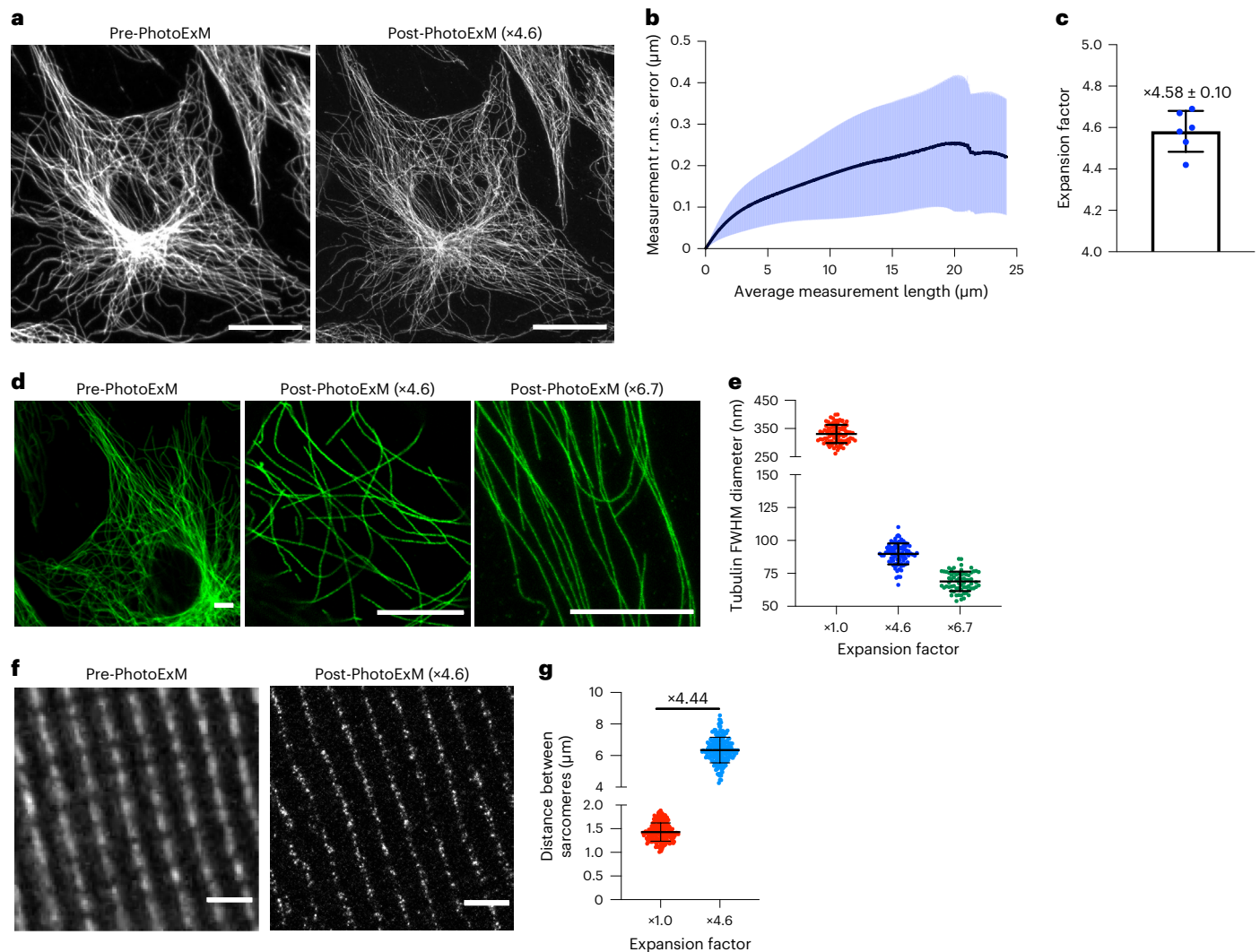
Fig. 2 | Isotropy and resolution of PhotoExM process. a, Representative images of C2C12 cells immunolabelled with α-tubulin before and after ×4.6 expansion. Scale bars, 10 μm. While the pre-expansion image is obtained from a single focal plane, the post-expansion images are a maximum intensity projection of five stacks of 0.71 μm apart. Images were acquired with a laser-scanning confocal microscope (Zeiss LSM 710) equipped with a ×20 NA = 1.0 water immersion objective at Nyquist sampling using a pinhole of 1.0 a.u. at λ = 488 nm. **b**, The r.m.s. error of the non-rigid registration process as a function of average measurement length. Black continuous line shows the average value, and the blue shaded area represents the standard deviation of 14 measurements obtained from six independent, expanded samples. **c**, Average expansion factor of six independent expanded samples. Data are presented as mean ± s.d. **d**, Representative images of microtubules of C2C12 cells before and after ×4.6 and ×6.7 expansions. Scale bars, 2 μm. All of the images show a single z stack. Imaging settings were water immersion objective = ×20, NA = 1.0, pinhole = 1.0 a.u. and λ = 488 nm at Nyquist sampling acquired with a laser-scanning confocal microscope (Zeiss LSM 710). **e**, FWHM diameter of microtubules measured before and after ×4.6 and ×6.7 expansions. N = 69, 88 and 90 microtubules for ×6.7 expanded, ×4.6 expanded and pre-PhotoExM samples, respectively, measured from 18 different cells from six different samples. **f**, Representative images of sarcomeres immunolabelled with α-actinin in 20-μm-thick longitudinal histological sections of the tibialis anterior muscle of 6-month-old male mice before and after ×4.6 expansion. Scale bars, 2 μm. While the pre-expansion image is a single z stack, the post-expansion image is a maximum intensity projection of eight stacks of 0.50 μm apart. Imaging settings were water immersion objective = ×60, NA = 1.2, pinhole = 1.2 a.u. and λ = 488 nm at Nyquist sampling (pixel size = 0.11 μm per pixel) acquired with a laser-scanning confocal microscope (Nikon A1R). **g**, Distance between sarcomeres before and after ×4.6 expansion. N = 192 and 207 sarcomeres for post-PhotoExM and pre-PhotoExM samples, respectively, measured from two independent muscle sections. Data are presented as mean ± s.d.

primarily rounded, and the fibronectin deposition did not significantly increase compared to day 1 (140 ± 181 μm³). At both days 1 and 3, we primarily observed punctate focal adhesions as determined by paxillin labelling with an almost complete absence of 3D mature matrix adhesions (3DMAs; Fig. 3e,f). The 3DMAs have characteristically thin, long morphologies and have been previously observed in vivo[29], as well as in hMSCs encapsulated in natural collagen-based hydrogels[30], but not in synthetic hydrogel cultures. By contrast, by day 7, hMSCs adopted highly spread morphologies with long lamellipodial protrusions (Fig. 3c)[31], and ~67% of the cells displayed 3DMAs that were exclusively

confined to protrusions (Fig. 3e,f). Strikingly, almost all 3DMAs exclusively aligned with the cellularly deposited fibronectin (334 ± 243 μm³; Fig. 3g), despite the presence of 1 mM of the fibronectin-mimetic RGD motif in the SPAAC hydrogels. These results suggest that in moderately stiff synthetic hydrogels (E′ = 7.0 ± 0.4 kPa), covalently tethered RGD at 1 mM is not sufficient to promote the formation of mature focal adhesions, and cell-deposited fibronectin is required for the formation of 3DMAs to support lamellipodial protrusions. The segmentation of focal adhesions is shown in Supplementary Fig. 8. However, even after seven days in culture, only ~50% and ~32% of the hMSCs deposited measurable
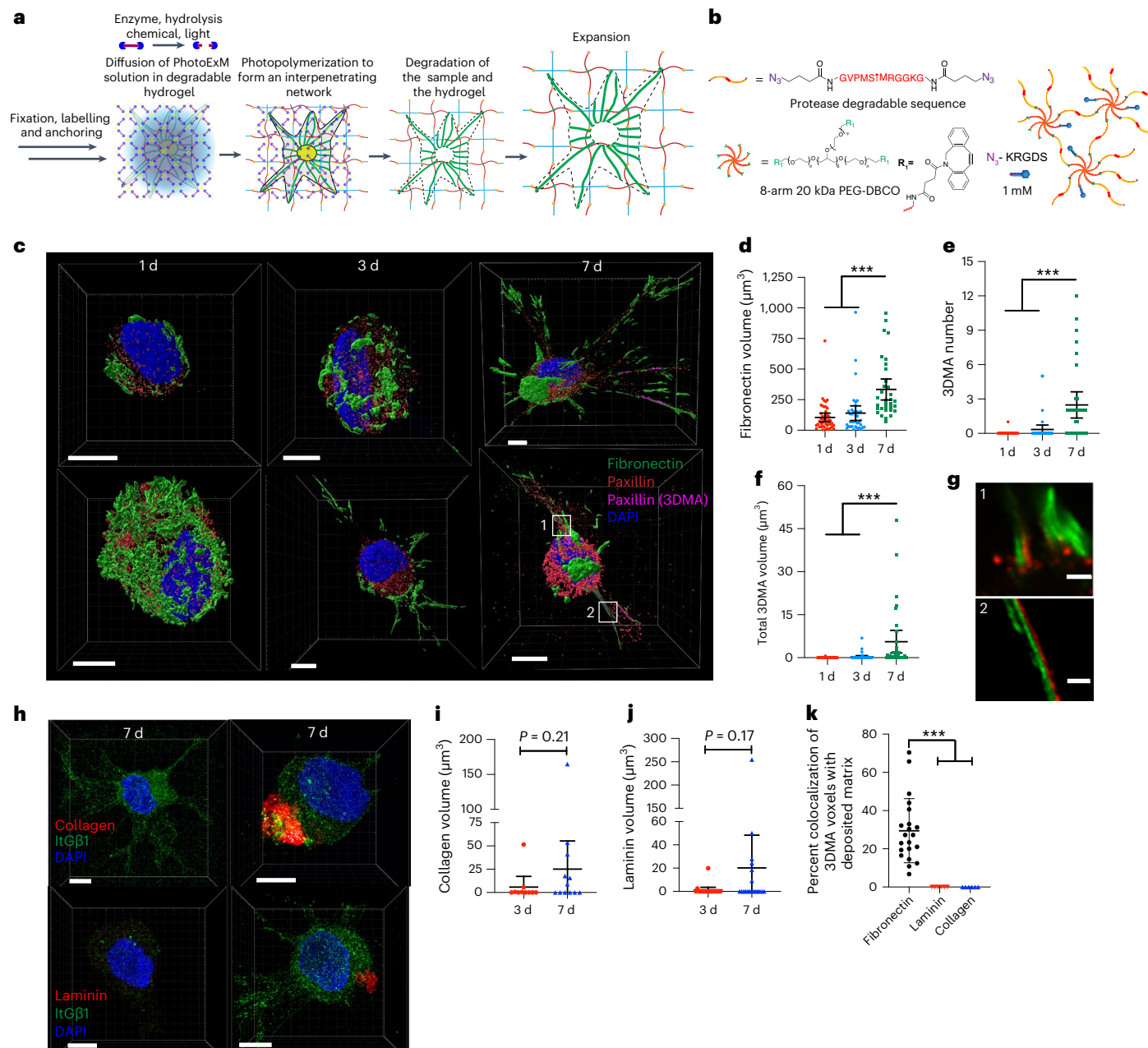
Fig. 3 | Super-resolution imaging of hMSCs and nascent deposited matrix in synthetic hydrogels. a, Schematic illustration of the GtG process. Cells cultured in 3D degradable hydrogels were fixed, labelled and anchored with acryloyl-X. Next, the PhotoExM formulation was diffused in degradable hydrogels, which is followed by the photopolymerization reaction to yield a temporary interpenetrating network. After degradation of the original 3D hydrogel and the biological sample within, samples were expanded with repeated H_2O washes to enable super-resolution imaging inside the 3D hydrogels. **b**, Chemical structures of the monomers used to fabricate protease-degradable 3D PEG hydrogels via SPAAC reaction. N_3-KRGDS, the fibronectin-mimetic adhesion sequence. **c**, Representative post-expansion images of hMSCs encapsulated in protease-degradable SPAAC hydrogels at one, three and seven days after encapsulation, immunolabelled with fibronectin and paxillin. Images were 3D reconstructed and segmented in IMARIS, which enabled a distinction between puncta and 3DMA paxillin adhesions. Scale bars, 9.2 μm. **d–f**, Quantification of fibronectin volume (**d**), 3DMA number (**e**) and total 3DMA volume (**f**) at one, three and seven days after encapsulation. $N = 33$ hMSCs (seven days post encapsulation, two

hydrogels), 38 hMSCs (three days post encapsulation, three hydrogels) and 46 hMSCs (one day post encapsulation, three hydrogels). Data are represented as mean ± 95% confidence interval (CI). ***$P < 0.001$ in a one-way analysis of variance (ANOVA) test ($P = 3.8 \times 10^{-6}$ and 3.8×10^{-8} in **d**, 2.3×10^{-7} and 2×10^{-10} in **e** and 1.1×10^{-9} and 8.6×10^{-7} in **f**). **g**, Zoomed-in images of insets in **c** showing the association of fibronectin and 3DMAs. Scale bar, 1 μm. Images are maximum intensity projections of five stacks at each 0.86 μm apart. **h**, Representative post-expansion images of hMSCs immunolabelled with collagen, laminin and ItGβ1 seven days after encapsulation. Images were 3D reconstructed in IMARIS. Scale bar, 9.2 μm. **i,j**, Quantification of collagen (**i**) and laminin (**j**) volumes at three and seven days after encapsulation. $N = 18$ hMSCs (three days post encapsulation) and 19 hMSCs (seven days post encapsulation). P values are obtained via a two-sided student's t-test. Data are presented as mean ± 95% CI. **k**, Percent volume colocalization of 3DMAs with fibronectin, collagen and laminin at seven days after encapsulation as measured in IMARIS. $N = 21$ fibronectin⁺ cells; $N = 6$ each for collagen and laminin⁺ cells. ***$P < 0.001$ in a one-way ANOVA test. $P = 1.8 \times 10^{-9}$. Data are presented as mean ± s.d.
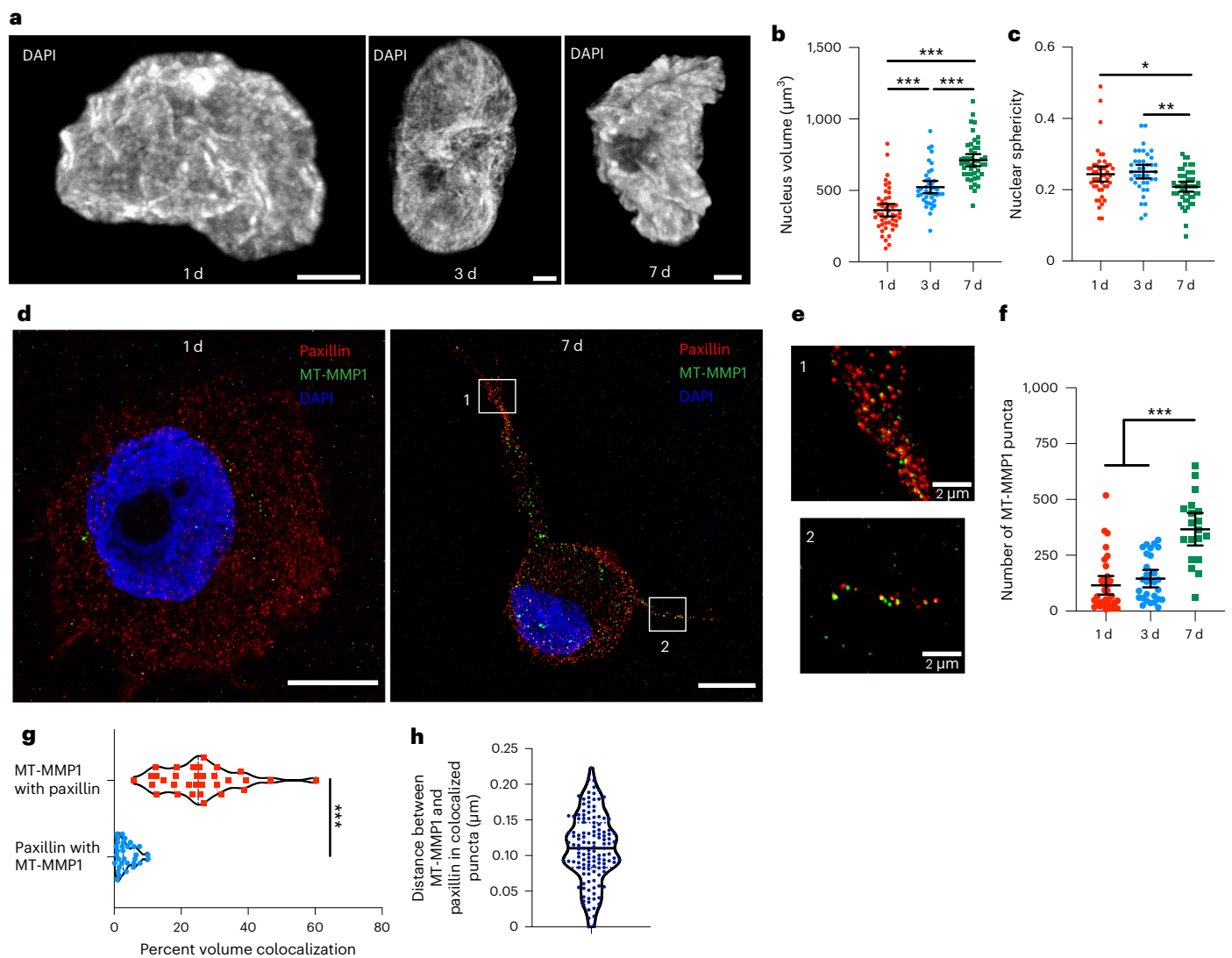
Fig. 4 | Nuclear architecture of hMSCs and evidence for cell-surface metalloproteinases. a, Representative images of expanded hMSC nuclei stained with DAPI at one, three and seven days after encapsulation. Images are 3D reconstructed with IMARIS. Scale bars, 3.3 μm. **b,c**, Quantification of the nucleus volume (**b**) and nuclear sphericity (**c**) at one, three and seven days after encapsulation. $N = 41–47$ nuclei from three independent encapsulations. Data are presented as mean ± 95% CI. *$P < 0.05$, **$P < 0.01$ and ***$P < 0.001$ in a one-way ANOVA test. $P = 2.7 \times 10^{-4}$, 3.3×10^{-5} and $<10^{-10}$ for the comparison between days 1 and 3, 3 and 7, and 1 and 7, respectively, in **b**. $P = 0.86$, 0.0012 and 0.03 for the comparison between days 1 and 3, 3 and 7, and 1 and 7, respectively, in **c. d**, Post-expansion representative images of hMSCs immunolabelled with MT-MMP1 and paxillin at one and seven days after encapsulation. Scale bars,

9.2 μm. Images are maximum intensity projections of ten stacks at each 0.86 μm apart. **e**, Zoomed-in images of insets in **d. f**, Quantification of MT-MMP1 puncta at one, three and seven days post encapsulation. $N = 19$ hMSCs (seven days post encapsulation, two hydrogels), 28 hMSCs (three days post encapsulation, two hydrogels) and 34 hMSCs (one day post encapsulation, three hydrogels). Data are presented as mean ± 95% CI; ***$P < 0.001$ in a one-way ANOVA test. $P = 0.56$, 2.5×10^{-7} and 0.00017 for the comparison between days 1 and 3, 3 and 7, and 1 and 7, respectively. **g**, Percent volume colocalization of MT-MMP1 and paxillin puncta measured with IMARIS. ***$P < 0.001$ in a student's *t*-test. $P < 10^{-10}$. **h**, Distance between MT-MMP1 and paxillin in colocalized puncta. $N = 131$ from 16 different cells in two independent encapsulations.

levels of collagen and laminin, respectively (Fig. 3h–j), and neither of these matrix proteins localized with 3DMAs (Fig. 3k). While nascently deposited collagen has been shown to influence hMSC behaviour and mechanosensing albeit at a lesser degree than fibronectin in synthetic hydrogels[26], these results suggest that fibronectin signals to hMSCs via 3DMAs.

Next, we analysed the nuclear volume and morphology of hMSCs in the same hydrogel system, as nuclear deformation is required for lamellipodial migration in constricted microenvironments (Fig. 4a,b)[32]. While nuclear volume increased with culture time (Fig. 4b), surprisingly, hMSCs had highly deformed nuclei by day 1 with very low sphericity (0.24 ± 0.07), even before formation of protrusions (Fig. 3c). This observation is contrary to what has been observed during the

lamellipodial migration in porous collagen-based hydrogels, where the formation of protrusions drives nuclear deformation through myosin II downstream signalling[33]. However, while collagen matrices that can restrict cell migration still have average pore sizes ranging from 1 to 5 μm (refs. 34,35), the SPAAC hydrogels prepared by step-growth polymerization of PEG chains have mesh sizes closer to 5–15 nm (ref. 36), limiting any cellular protrusions prior to MMP-mediated degradation. Therefore, passive pushing of the elastic matrix in moderately stiff ($E' = 7.0$ kPa) synthetic hydrogels may be sufficient for nuclear deformation[32], even in the absence of protrusions, through mechanisms that do not involve mature focal adhesion formation and their downstream mechanotransduction signalling.

Since we observed highly elongated hMSCs with long, lamellipodia-like protrusions at day 7, rather than volumetrically expanded, amoeboid cellular morphologies[31], we hypothesized that hMSCs may use membrane-bound metalloproteinases to locally degrade synthetic hydrogels to enlarge their protrusions, in addition to soluble MMPs. We focused on the membrane-type matrix metalloproteinase I (MT-MMP1), which is known to promote protrusion and lamellipodial migration in constricted microenvironments in many cancer cells[37], but has not been observed in hMSCs. In fact, hMSCs displayed bright MT-MMP1 puncta (Fig. 4d), suggesting the presence of membrane-bound proteolytic activity. The number of MT-MMP1 puncta was significantly higher at day 7 (367 ± 151), where hMSCs adopted a highly spread morphology compared to day 1 (115 ± 119) or day 3 (145 ± 101; Fig. 4e). MT-MMP1 was not exclusively confined to the protrusions (Fig. 4d), as previously observed in HT-1080 fibrosarcoma and MDA-MB-231 breast cancer cell lines[37]. Thus, it may be that MT-MMP1 contributes both to the extension and enlargement of protrusions, as well as expansion of the hMSC main body. Furthermore, we serendipitously found a significant association between nascent focal adhesions (punctate paxillin staining) and MT-MMP1 puncta (Fig. 4f,g), but not between nascent focal adhesions and 3DMAs. The interaction between MT-MMP1 and focal adhesion is likely multifaceted, as it has been shown to promote ECM degradation[38] or the degradation of the focal adhesion itself[39]. However, we were able to resolve that paxillin and MT-MMP1 puncta associate, but the FWHM of their signal separates by 111 ± 47 nm, demonstrating the capabilities of the GtG technique to answer such questions. In summary, GtG enables the super-resolution imaging of spatially resolved features embedded in 3D biomaterials and allows the interpretation of cellular features and outside-in signalling with nanoscale resolution.

Outlook

While synthetic hydrogels have been extensively used as biomimetic, 3D cell culture platforms, the nanoscale interpretation of cell behaviour, cell–matrix interactions and downstream signalling cascades are largely unavailable due to the difficulties in carrying out optically deep, high-resolution imaging in these microenvironments. Given that ECM-sensing focal adhesions can be structurally and compositionally different in 3D materials compared to 2D (ref. 40), and combined with the various cell polarization states and migratory behaviour in 3D materials (ref. 41), alternative mechanisms of cell–matrix interactions and downstream signalling may be present and potentially more relevant in predicting in vivo behaviour. By enabling the super-resolution imaging of cells embedded within biomaterial matrices, PhotoExM can improve the field's understanding of how cells behave in 3D microenvironments and in parallel advance biomaterial design to better meet cellular needs. Furthermore, as an ExM technique, PhotoExM offers a simple and robust complementary method that can circumvent some of the limitations of monomer diffusion, oxygen inhibition and hydrogel fragility post expansion, and enables the premixing of the formulation. While our use of UV photoinitiators may limit the thickness of certain tissue samples that can be homogeneously expanded with PhotoExM to ~50 µm, our method can be easily adapted for use with visible and near-infrared photoinitiators to enable the PhotoExM of 100-µm-thick tissue samples[42].

As a proof of concept, we demonstrate cell-nascent protein interactions in three dimensions as an area of growing interest, especially with respect to the dynamic reciprocity of cell–matrix signalling and its effects on mechanosensing[26] and differentiation[27]. PhotoExM can provide a method for studying the effects of initial hydrogel-provided cues (stiffness, matrix) on cells versus cellular remodelling of the local matrix properties, especially as a function of culture time. By focusing on the cell–matrix interface, we distinguished the differences between nascent and mature focal adhesions, the latter almost exclusively associated with hMSC-deposited fibronectin. As fibronectin is

an ~1,000-fold more potent mediator of integrin signalling compared to RGD[43], our data suggest that RGD sequestration is not sufficient for focal adhesion maturation in synthetic hydrogels. This further complicates the role of RGD, as the absence of RGD causes cell death through anoikis[44], suggesting that initial cell–matrix binding is a prerequisite for nascent ECM deposition. However, RGD may competitively bind to an array of various integrins and inhibit signalling following fibronectin secretion[45]. Temporal loss of function studies either via conditional knockouts or hydrogel functionalization with photodegradable adhesion ligands[46,47] in combination with PhotoExM may help elucidate the answer to these questions. Finally, PhotoExM provides a method to accurately monitor nuclear shape and chromatin architecture in 3D microenvironments, which have been extensively studied in two dimensions and are known to regulate cell fate and transcriptional states[48,49]. However, less is known about the nucleus in three dimensions (ref. 50), and studies to date have been limited by resolution. Of further note, since ExM is compatible with RNA imaging[7], PhotoExM might be tailored in the future to accurately characterize the subcellular and cellular heterogeneities of transcriptional states in 3D microenvironments, which remain largely unknown.

Online content

Any methods, additional references, Nature Portfolio reporting summaries, source data, extended data, supplementary information, acknowledgements, peer review information; details of author contributions and competing interests; and statements of data and code availability are available at https://doi.org/10.1038/s41563-023-01558-5.

References

1. Chen, F., Tillberg, P. W. & Boyden, E. S. Expansion microscopy. *Science* **347**, 543–548 (2015).
2. Chozinski, T. J. et al. Expansion microscopy with conventional antibodies and fluorescent proteins. *Nat. Methods* **13**, 485–488 (2016).
3. Tillberg, P. W. et al. Protein-retention expansion microscopy of cells and tissues labeled using standard fluorescent proteins and antibodies. *Nat. Biotechnol.* **34**, 987–992 (2016).
4. Truckenbrodt, S. et al. X10 expansion microscopy enables 25-nm resolution on conventional microscopes. *EMBO Rep.* **19**, e45836 (2018).
5. Zhao, Y. et al. Nanoscale imaging of clinical specimens using pathology-optimized expansion microscopy. *Nat. Biotechnol.* **35**, 757–764 (2017).
6. Alon, S. et al. Expansion sequencing: spatially precise in situ transcriptomics in intact biological systems. *Science* **371**, aax2656 (2021).
7. Chen, F. et al. Nanoscale imaging of RNA with expansion microscopy. *Nat. Methods* **13**, 679–684 (2016).
8. Asano, S. M. et al. Expansion microscopy: protocols for imaging proteins and RNA in cells and tissues. *Curr. Protoc. Cell Biol.* **80**, e56 (2018).
9. Gao, R. et al. A highly homogeneous polymer composed of tetrahedron-like monomers for high-isotropy expansion microscopy. *Nat. Nanotechnol.* **16**, 698–707 (2021).
10. Tibbitt, M. W., Kloxin, A. M., Sawicki, L. A. & Anseth, K. S. Mechanical properties and degradation of chain and step-polymerized photodegradable hydrogels. *Macromolecules* **46**, 2785–2792 (2013).
11. Cramer, N. B. & Bowman, C. N. Kinetics of thiol–ene and thiol–acrylate photopolymerizations with real-time Fourier transform infrared. *J. Polym. Sci. A Polym. Chem.* **39**, 3311–3319 (2001).
12. O'Brien, A. K., Cramer, N. B. & Bowman, C. N. Oxygen inhibition in thiol–acrylate photopolymerizations. *J. Polym. Sci. A Polym. Chem.* **44**, 2007–2014 (2006).

13. Hoffman, A. S. Hydrogels for biomedical applications. *Adv. Drug Deliv. Rev.* **64**, 18–23 (2012).

14. Caliari, S. R. & Burdick, J. A. A practical guide to hydrogels for cell culture. *Nat. Methods* **13**, 405–414 (2016).

15. Rosales, A. M. & Anseth, K. S. The design of reversible hydrogels to capture extracellular matrix dynamics. *Nat. Rev. Mater.* **1**, 15012 (2016).

16. Rydholm, A. E., Bowman, C. N. & Anseth, K. S. Degradable thiol-acrylate photopolymers: polymerization and degradation behavior of an in situ forming biomaterial. *Biomaterials* **26**, 4495–4506 (2005).

17. Ye, S., Cramer, N. B. & Bowman, C. N. Relationship between glass transition temperature and polymerization temperature for cross-linked photopolymers. *Macromolecules* **44**, 490–494 (2011).

18. Jones, B. et al. Curing behavior, chain dynamics, and microstructure of high T_g thiol-acrylate networks with systematically varied network heterogeneity. *Polymer* **205**, 122783 (2020).

19. Lee, H. et al. Tetra-gel enables superior accuracy in combined super-resolution imaging and expansion microscopy. *Sci. Rep.* **1**, 16944 (2021).

20. Flory, P. J. Molecular size distribution in three dimensional polymers. I. Gelation. *J. Am. Chem. Soc.* **63**, 3083–3090 (1941).

21. Fairbanks, B. D., Schwartz, M. P., Bowman, C. N. & Anseth, K. S. Photoinitiated polymerization of PEG-diacrylate with lithium phenyl-2,4,6-trimethylbenzoylphosphinate: polymerization rate and cytocompatibility. *Biomaterials* **30**, 6702–6707 (2009).

22. Hell, S. W. Far-field optical nanoscopy. *Science* **316**, 1153–1158 (2007).

23. Goulding, D., Bullard, B. & Gautel, M. A survey of in situ sarcomere extension in mouse skeletal muscle. *J. Muscle Res. Cell Motil.* **18**, 465–472 (1997).

24. Mauro, A. Satellite cell of skeletal muscle fibers. *J. Biophys. Biochem. Cytol.* **9**, 493–495 (1961).

25. Blatchley, M. R. et al. In situ super-resolution imaging of organoids and extracellular matrix interactions via photo-transfer by allyl sulfide exchange-expansion microscopy (PhASE-ExM). *Adv. Mat.* **18**, 2109252 (2022).

26. Loebel, C., Mauck, R. L. & Burdick, J. A. Local nascent protein deposition and remodelling guide mesenchymal stromal cell mechanosensing and fate in three-dimensional hydrogels. *Nat. Mater.* **18**, 883–891 (2019).

27. Ferreira, S. A. et al. Bi-directional cell-pericellular matrix interactions direct stem cell fate. *Nat. Commun.* **9**, 4049 (2018).

28. Brown, T. E. et al. Secondary photocrosslinking of click hydrogels to probe myoblast mechanotransduction in three dimensions. *J. Am. Chem. Soc.* **140**, 11585–11588 (2018).

29. Cukierman, E., Pankov, R., Stevens, D. R. & Yamada, K. M. Taking cell-matrix adhesions to the third dimension. *Science* **294**, 1708–1712 (2001).

30. Li, C. W., Lau, Y. T., Lam, K. L. & Chan, B. P. Mechanically induced formation and maturation of 3D-matrix adhesions (3DMAs) in human mesenchymal stem cells. *Biomaterials* **258**, 120292 (2020).

31. Yamada, K. M. & Sixt, M. Mechanisms of 3D cell migration. *Nat. Rev. Mol. Cell Biol.* **20**, 738–752 (2019).

32. Friedl, P., Wolf, K. & Lammerding, J. Nuclear mechanics during cell migration. *Curr. Opin. Cell Biol.* **23**, 55–64 (2011).

33. Cramer, L. P. Forming the cell rear first: breaking cell symmetry to trigger directed cell migration. *Nat. Cell Biol.* **12**, 628–632 (2010).

34. Wolf, K. et al. Collagen-based cell migration models in vitro and in vivo. *Semin. Cell Dev. Biol.* **20**, 931–941 (2009).

35. Wolf, K. et al. Physical limits of cell migration: control by ECM space and nuclear deformation and tuning by proteolysis and traction force. *J. Cell Biol.* **201**, 1069–1084 (2013).

36. Rehmann, M. S. et al. Tuning and predicting mesh size and protein release from step growth hydrogels. *Biomacromolecules* **18**, 3131–3142 (2017).

37. Wolf, K. et al. Multi-step pericellular proteolysis controls the transition from individual to collective cancer cell invasion. *Nat. Cell Biol.* **9**, 893–904 (2007).

38. Woskowicz, A. M., Weaver, S. A., Shitomi, Y., Ito, N. & Itoh, Y. MT-LOOP-dependent localization of membrane type I matrix metalloproteinase (MT1-MMP) to the cell adhesion complexes promotes cancer cell invasion. *J. Biol. Chem.* **288**, 35126–35137 (2013).

39. Shofuda, T. et al. Cleavage of focal adhesion kinase in vascular smooth muscle cells overexpressing membrane-type matrix metalloproteinases. *Arterioscler. Thromb. Vasc. Biol.* **24**, 839–844 (2004).

40. Paul, N. R. et al. α5β1 integrin recycling promotes Arp2/3-independent cancer cell invasion via the formin FHOD3. *J. Cell Biol.* **210**, 1013–1031 (2015).

41. Petrie, R. J. & Yamada, K. M. Multiple mechanisms of 3D migration: the origins of plasticity. *Curr. Opin. Cell Biol.* **42**, 7–12 (2016).

42. Xiao, P. et al. Visible light sensitive photoinitiating systems: recent progress in cationic and radical photopolymerization reactions under soft conditions. *Prog. Polym. Sci.* **41**, 32–66 (2015).

43. Hautanen, A., Gailit, J., Mann, D. M. & Ruoslahti, E. Effects of modifications of the RGD sequence and its context on recognition by the fibronectin receptor. *J. Biol. Chem.* **264**, 1437–1442 (1989).

44. Benoit, D. S. W. et al. Integrin-linked kinase production prevents anoikis in human mesenchymal stem cells. *J. Biomed. Mater. Res. A* **81**, 259–268 (2007).

45. Hennessy, K. M. et al. The effect of RGD peptides on osseointegration of hydroxyapatite biomaterials. *Biomaterials* **29**, 3075–3083 (2008).

46. Azagarsamy, M. A. & Anseth, K. S. Wavelength-controlled photocleavage for the orthogonal and sequential release of multiple proteins. *Angew. Chem. Int. Ed.* **52**, 13803–13807 (2013).

47. Grim, J. C. et al. A reversible and repeatable thiol–ene bioconjugation for dynamic patterning of signaling proteins in hydrogels. *ACS Cent. Sci.* **4**, 909–916 (2018).

48. Alisafaei, F., Jokhun, D. S., Shivashankar, G. V. & Shenoy, V. B. Regulation of nuclear architecture, mechanics, and nucleocytoplasmic shuttling of epigenetic factors by cell geometric constraints. *Proc. Natl Acad. Sci. USA* **116**, 13200–13209 (2019).

49. Walker, C. J. et al. Nuclear mechanosensing drives chromatin remodelling in persistently activated fibroblasts. *Nat. Biomed. Eng.* **5**, 1485–1499 (2021).

50. Cosgrove, B. D. et al. Nuclear envelope wrinkling predicts mesenchymal progenitor cell mechano-response in 2D and 3D microenvironments. *Biomaterials* **270**, 120662 (2021).

Methods

Ethical compliance statement

Mice were bred and housed according to National Institutes of Health guidelines for the ethical treatment of animals in a pathogen-free facility at the University of Colorado at Boulder. The University of Colorado Institutional Animal Care and Use Committee approved all animal protocols and procedures.

Fabrication and characterization of PhotoExM hydrogels

Stock solutions of NaAc (33 wt%), PEGdiAcM ($M_n = 600$ g mol^{-1}, 25 wt%), AcM (40 wt%), 8-arm, 10 kDa PEG-SH (25 wt%) and LAP (2 wt%) in PBS containing additional 2 M NaCl were premixed and stored in the dark to obtain the PhotoExM formulations shown in Supplementary Table 2. PhotoExM formulations were sandwiched between two hydrophobic glass slides coated with Rain-X and separated with 400 µm rubber spacers on a lab benchtop. The solutions were irradiated with $\lambda = 365$ nm, $I = 4.5$ mW cm^{-2} light for 70 seconds to obtain the PhotoExM hydrogels. Following polymerization, the PhotoExM hydrogels were detached from the glass slides and transferred into a petri dish with 5.5 cm diameter, and the expansion was carried out by four 20 min washes with deionized H$_2$O.

For the determination of the storage moduli (G'; Fig. 1b,f), PhotoExM formulations were in situ polymerized on a TA Instruments Ares RH3 rheometer equipped with a UV light guide accessory and coupled with the Omnicure 1000 light source ($\lambda = 365$ nm, $I = 4.5$ mW cm^{-2}). The storage modulus (G') of the hydrogels was measured using an oscillatory strain with an amplitude of 1% and a frequency of 1 Hz. For the determination of the expansion factors, three different methods were used. (1) PhotoExM hydrogels were transferred onto a mesh grid (Fig. 1d), and their pre- and post-expansion dimensions were measured. (2) The pre- and post-expansion masses (m_i and $m_{swollen}$, respectively) of the hydrogels were measured, and the expansion factor was calculated using the formula $= (m_{swollen}/m_i)^{1/3}$ (Fig. 1c). (3) The pre- and post-expansion microtubule images used in non-rigid registration experiments (Fig. 2a) were additionally used to verify the expansion factors (Fig. 2c).

Non-rigid registration experiments and determination of the resolution

Non-rigid registration. C2C12 cells (ATCC catalog no. CRL-1772) were grown on 12 mm glass coverslips coated with gelatin until reaching subconfluency (~90%). Cells were cultured at 5% CO$_2$ and 37 °C in high glucose DMEM growth medium with 20 v/v% fetal bovine serum (FBS), 1 v/v% sodium pyruvate, 1 v/v% L-glutamine, 1% v/v penicillin–streptomycin and 0.1 v/v% Fungizone. Next, C2C12 cells were first extracted with cytoskeletal stabilization (PEM) buffer for 30 s (ref. 2), and fixed with PEM buffer containing 3.2 v/v% paraformaldehyde (PFA) and 0.1 v/v% glutaraldehyde for 10 min at room temperature. Samples were briefly washed with PBS, and excess glutaraldehyde was reduced with 10 mM NaBH$_4$ in PBS for 5 min. Sample were washed three times with PBS (10 min each) and permeabilized and blocked for 30 min in PBS containing 3 w/v% bovine serum albumin (BSA) and 0.5 w/v% Triton-X. Samples were first treated with α-tubulin primary antibody for 45 min in PBS containing 3 w/v% BSA and 0.5 w/v% Triton-X, washed three times with PBS (10 min each). Then the samples were treated with Alexa Fluor Plus 488 secondary antibody for 45 min in PBS containing 3 w/v% BSA and 0.5 w/v% Triton-X, and washed three times with PBS. Immunolabelling was carried out at room temperature. Pre-expansion imaging was carried out using a Zeiss LSM 710 confocal microscope equipped with a ×20 NA = 1.0 water immersion objective. Imaging settings of pinhole = 1.0 a.u., $\lambda = 488$ nm and z stack = 0.71 µm at Nyquist sampling were used. Zeiss ZEN software was used to acquire the images.

Next, samples were anchored by reacting with 0.1 mg ml^{-1} acryloyl-X in PBS for 3 h at room temperature. Samples were washed three times with PBS (10 min each) and transferred between two Rain-X-coated glass slides 400 µm apart, and PhotoExM formulations (×4.6 expansion) were diffused into the sample for 10 min at room temperature. Next, PhotoExM hydrogels were polymerized as described in 'Fabrication and characterization of hydrogels' in Methods, detached from the glass slides and digested with digestion buffer containing Proteinase K (8 U ml^{-1})[1] overnight at room temperature. The next day, samples were expanded with four deionized H$_2$O washes (20 min each) and mounted on poly-L-lysine-coated glass, and identical areas, visualized pre-expansion, were located and imaged. Post-expansion images were obtained with identical settings to those used in pre-expansion imaging. Samples were kept entirely submerged in H$_2$O throughout the imaging. In total, 14 cells from six different samples were used for the non-rigid registration process. This protocol can be generalized to carry out the PhotoExM of monolayer cell cultures.

Non-rigid registration was carried out as previously reported[1]. Briefly, pre- and post-expansion images were first overlapped using the TurboReg plug-in in ImageJ[51], and then registered using a B-spline registration algorithm in MATLAB[52]. For each registration, at least 15 clearly defined points (that is, intersections) were chosen to carry out the analysis. The error vectors of the resulting algorithm are shown in Supplementary Fig. 4a, which is used to calculate the average r.m.s. error as a function of measurement distance for the PhotoExM process (Fig. 2b).

Sample resolution. To determine the resolution, the same microtubule images used in the non-rigid registration experiments were used, as they provide an accurate characterization of the expansion factors. In addition to the ×4.6 expanded samples, six more α-tubulin immunolabelled C2C12 samples that were expanded ×6.7 were used in these experiments. Line intensity profiles in single z stacks were manually drawn perpendicular to the microtubules in ImageJ and curve-fitted using a Gaussian approximation, and the FWHM of the Gaussians were reported as the resolution (Fig. 2e shows the images and Supplementary Fig. 4b shows the line intensity profiles).

PhotoExM of tissue sections and muscle myofibres. Tibialis anterior muscles of six-month-old male mice (C57Bl/6J) were isolated and fixed with 4 w/v% PFA for 2 h. Muscle was rinsed with PBS for 5 min and soaked in 30 w/v% sucrose overnight at 4 °C. Tissue was then embedded in optimal cutting temperature compound on dry ice, cryosectioned (20 µm thick) in the longitudinal direction and immobilized on gelatin-coated coverslips. After washing with PBS, sections were fixed with 4 w/v% PFA at room temperature for 5 min, and washed once more with PBS for 5 min. For antigen retrieval, samples were soaked in EDTA buffer at pH 8.0 and boiled in a pressure cooker for 6 min. Then, the samples were left at room temperature for 20 min, washed three times with PBS (5 min each) and blocked with 2 w/v% BSA and 0.125 w/v% Triton-X in PBS for 30 min at room temperature. The sections were immunolabelled with α-actinin primary antibody for 1 h at room temperature in 2 w/v% BSA and 0.125 w/v% Triton-X in PBS. After five PBS washes (5 min each), samples were incubated with the Alexa Fluor Plus 488 secondary antibody for 1 h and washed three times with PBS (5 min each). Pre-expansion imaging was carried out using a Nikon A1R confocal microscope equipped with a ×60 NA = 1.2 water immersion objective. Imaging settings of pinhole = 1.2 a.u., $\lambda = 488$ nm and z stack = 1 µm at Nyquist sampling (pixel size = 0.11 µm per pixel) were used.

Next, sections were treated with 0.1 mg ml^{-1} acryloyl-X in PBS overnight at room temperature. Then, sections were washed three times with PBS (10 min each) and transferred between two Rain-X-coated glass slides at 400 µm apart, and PhotoExM formulations (×4.6 expansion) were diffused into the sample for 15 min at room temperature. PhotoExM hydrogels were polymerized as described in 'Fabrication and characterization of PhotoExM hydrogels' in Methods, detached from the glass slides and digested with digestion buffer containing Proteinase K (16 U ml^{-1}) overnight at 37 °C. The next day, samples were expanded with four deionized H$_2$O washes (20 min each), mounted on poly-L-lysine-coated glass chambers suitable for inverted microscopes

(Ibidi, 81158) and imaged with identical settings as those used to obtain pre-expansion images. This protocol can be generalized to carry out the PhotoExM of thin tissue sections. In total, 24 different areas from two different sections were imaged for both pre- and post expansion (Fig. 2f). The average sarcomere lengths were quantified from two-peak Lorentzian approximations of the line profiles (ImageJ) perpendicular to the α-actinin labels (Fig. 2g).

To obtain post-expansion images of muscle stem cells on isolated myofibres (Supplementary Fig. 5), myofibres from the tibialis anterior muscles of adult mice (3–6 months) were isolated, fixed and immuno-labelled using previously established methods[53]. For the immunolabel-ling, Pax7 (mouse, Developmental Studies Hybridoma Bank, 1:250), dystrophin (rabbit, Abcam, 15277, 1:63) and laminin (rabbit, Sigma Aldrich, L9393, 1:63) primary antibodies and Alexa Fluor 488 (Thermo Fisher) and Alexa Fluor 546 (Thermo Fisher) secondary antibodies were used. The samples were immobilized on gelatin-coated 12 mm coverslips and treated with 0.1 mg ml^{-1} acryloyl-X for 6 hours, and then washed three times with PBS. Samples were permeated with the Photo-ExM formulation enabling ×4.6 expansion for 15 minutes, as described above, before 70 s of photopolymerization. The samples were digested overnight and expanded using four H$_2$O washes (20 min each). Next, nuclei were labelled using DAPI (1:500) for 1 h in H$_2$O. Samples were washed three more times with H$_2$O, mounted on poly-L-lysine-coated glass and imaged using a Zeiss LSM 710 confocal microscope equipped with a ×20 NA = 1.0 water immersion objective. Imaging settings of pinhole = 2 a.u., λ = 488 and 456 nm and z stack = 1.72 μm at Nyquist sampling were used. The brightness and contrast of each channel was independently adjusted to better visualize the features prior to the generation of the merged images in ImageJ (Supplementary Fig. 5).

GtG transfer experiments
Fabrication of MMP-degradable SPAAC hydrogels. Synthesis of 8-arm, 20 kDa PEG-DBCO, N$_3$-GVPMSMRGGK(N$_3$)G-N$_3$ and N$_3$-KRGDS were carried out as previously reported by our group[22]. SPAAC hydro-gels were fabricated by mixing precursor solutions of PEG-DBCO (5 wt%), N$_3$-GVPMSMRGGK(N$_3$)G-N$_3$ and N$_3$-KRGDS (1 mM) in PBS, pH 7.4 at room temperature. We ensured that the final formulation contained stochiometric amounts of dibenzocyclooctyne (DBCO) and N$_3$ groups by using rheology in the presence of 1 mM LAP, as excess DBCO groups can undergo a radical mediated photocrosslinking reaction[28], which can interfere with the PhotoExM polymerization process. The hydrogel storage modulus (G') was measured in situ on a TA Instruments Ares RH3 rheometer using an 1% oscillatory strain and a frequency of 1 Hz (Supplementary Fig. 6c). The G' values were converted to Young's modulus (E') using the equation $E' = 2G'(1 + v)$, where v is Poisson's ratio and assumed to be 0.5 for an incompressible material.

Encapsulation and labelling of hMSCs. The hMSC isolation from human bone marrow aspirate and serial expansion was carried out using previous protocols[54,55]. The hMSCs were isolated from human bone marrow aspirate purchased from Lonza; the bone marrow was isolated from an 18-year-old black female. The hMSCs at P3 (5×10^5 cells ml^{-1}) in PBS, pH 7.4 were mixed with the SPAAC hydrogel formulation (1×10^6 cells ml^{-1}) described in 'Fabrication of MMP-degradable SPAAC hydrogels' in Methods, and the solutions (15 μl per hydrogel) were immediately sandwiched between two Rain-X-coated slides, 400 μm apart. Before encapsulation, the pH values of the SPAAC hydrogels were adjusted to 7.4 with 0.5 M NaOH, as N$_3$-GVPMSMRGGK(N$_3$)G-N$_3$ incorporation acidifies the formulation, lowering cell viability. Hydro-gels were polymerized for 7 min and transferred into a 1 ml DMEM low glucose media containing 10 v/v% FBS, 1 v/v% penicillin–streptomycin and 0.1 v/v% Fungizone in a 24-well plate. The viability of hMSCs (>90%) was assessed 24 h after polymerization using calcein AM as the live cell reporter and ethidium homodimer-1 as the dead cell reporter (Supplementary Fig. 6a,b).

On one, three or seven days after encapsulation, samples were fixed with 10 v/v% formalin in PBS (pH 7.0) for 30 min at room tem-perature and washed three times with PBS (10 min each). Samples immunolabelled with fibronectin/paxillin, collagen/integrin β1 (ItGβ1) and laminin/ItGβ1 were permeabilized and blocked with 2 w/v% BSA and 0.2 w/v% Triton-X in PBS at room temperature. Samples immunolabelled with MT-MMP1/paxillin were permeabilized with 0.1 w/v% Tween 20 for 1 h, and then blocked with 2 w/v% BSA for 1 h at room temperature. Next, samples were treated with the following primary antibodies overnight at 4 °C either in the presence (MT-MMP$^-$ samples) or absence (MT-MMP$^+$ samples) of 0.2 w/v% Triton-X in PBS containing 2 w/v% BSA: paxillin (Y113, abcam, 1:150), fibronectin (IST-9, abcam, 1:250), collagen (ab34710, abcam, 1:200), laminin (ab11575, abcam, 1:200), integrin β1 (9EG7, BD Pharmingen, 1:250) and MT-MMP1 (C-9, SCBT, 1:100). The next day, sam-ples were washed three times with PBS (10 min each) and treated with secondary antibodies (Alexa Fluor 488, Alexa Fluor Plus 488 and Alexa Fluor Plus 594, 1:250) in PBS containing 2 w/v% BSA and with or without 0.2 w/v% Triton-X, and washed again three times with PBS (10 min each).

Expansion of hMSCs via GtG transfer. Samples were treated with 0.1 mg ml^{-1} acryloyl-X in PBS overnight at room temperature and washed three times with PBS. Next, samples were dried and incubated two times with 250 μl of PhotoExM formulation (×4.6 expansion; Sup-plementary Table 2) for 30 min each at room temperature. After two incubations, the samples were transferred into a 5.5 cm petri dish, residual liquid was wicked away with a Kimwipe and a Rain-X-coated 12 mm glass coverslip was placed on top of the samples. The samples were irradiated with λ = 365 nm, I = 4.5 mW cm^{-2} light for 70 seconds to obtain an interpenetrating network composed of SPAAC and PhotoExM hydrogels. In these experiments, the PhotoExM solution used for the second incubation was stored, and later used as the first incubation in the subsequent experiments. Next, samples and the SPAAC hydrogels were digested with buffer containing Protein-ase K (8 U ml^{-1}) overnight at 37 °C. Samples were expanded once with a 20 min deionized H$_2$O wash, stained with DAPI (1:500) for 1 h in deionized H$_2$O and washed two more times with deionized H$_2$O (20 min each) to achieve the final expansion. The sample expansion factor was approximately ×3.2 due to the ~30% shrinkage of SPAAC hydrogels in size during the incubation with PhotoExM formulation (Supplementary Fig. 6d).

Approximation of diffusion timescales of PhotoExM formulation into the SPAAC hydrogels. To calculate the diffusion of the PhotoExM formulation, we used 8-arm, 10 kDa PEG-SH as the limiting component due to its larger size. We assumed its hydrodynamic radius (R_h) to be 2.30 nm, which was reported for a linear 10 kDa PEG[56], and likely to be smaller as star-shaped polymers have smaller hydrodynamic radii compared to linear polymers with identical molecular weight[57]. The diffusion coefficient of 10 kDa PEG is calculated from the Stokes–Einstein equation:

$$D_0 = \frac{k_B T}{6\pi\eta R_s} = 1.38 \times 10^{-6} \text{ cm}^2\text{ s}^{-1} \qquad (1)$$

where k_B is the Boltzmann constant (1.38×10^{-23} J K^{-1}), T is the tempera-ture (300 K), η is the dynamic viscosity of water at 300 K (6.92×10^{-4} Pa s^{-1}) and R_s is the solute size, assumed to be equal to R_h (2.30 nm).

Next, to determine the average mesh size of the SPAAC networks, we determined the molecular weight between crosslinks ($\bar{M}_c$) via the Flory–Rehner equation:

$$\frac{1}{\bar{M}_c} = \frac{2}{\bar{M}_n} - \frac{\frac{\bar{v}}{V_1}\left(\ln(1-v_2) + v_2 + X_1 v_2^2\right)}{v_2^{\frac{1}{3}} - \frac{v_2}{2}} = 4{,}111 \text{ g mol}^{-1} \qquad (2)$$

where $\bar{M}_n$ is the number average molecular weight of the hydrogel monomers (5,044 g mol^{-1} for this SPAAC hydrogel), V_1 is the solvent molar volume (18 cm^3 mol^{-1} for H$_2$O), v_2 is the polymer volume fraction in the equilibrium swollen hydrogel (assumed to be 0.05), $\bar{v}$ is the specific volume of the polymer (0.89) and X_1 is the interaction parameter (0.426 for PEG)[58].

Then, the r.m.s. end-to-end distance of the polymers in the unperturbed state $\sqrt{\langle r_0^2 \rangle}$ was calculated:

$$\sqrt{\langle r_0^2 \rangle} = l C_n^{1/2} n^{1/2} = 4.89 \, \text{nm} \tag{3}$$

where l is the average bond length (0.146 nm for PEG)[59], C_n is the polymer characteristic ratio (4 for PEG)[60] and n is number of bonds in the crosslink (280 for this SPAAC hydrogel). Then, the average mesh size (ξ) is

$$\xi = v_2^{-1/3} \sqrt{\langle r_0^2 \rangle} = 13.3 \, \text{nm}. \tag{4}$$

Then, we can calculate the diffusion coefficient (D_g) in the hydrogels as follows:

$$D_g = D_0 \left(\left(1 - \frac{R_s}{\xi}\right) e^{\left(-Y\left(\frac{v_2}{1-v_2}\right)\right)} \right) = 1.08 \times 10^{-6} \, \text{cm}^2 \, \text{s}^{-1} \tag{5}$$

where Y is the ratio of the critical volume required for a successful translational movement of the solute to the average free volume per liquid molecule and is assumed to be 1 (ref. [61]). Then assuming Fick's law, the characteristic diffusion times can be approximated as follows:

$$\frac{M_t}{M_0} \approx 2 \sqrt{\frac{D_g t}{\pi \delta^2}} \tag{6}$$

where M_t is the solute concentration diffused after time t, M_0 is the initial solution concentration and δ is the half thickness of the SPAAC hydrogels (200 µm). When $M_t = M_0$, $t = 291$ s, which is substantially shorter than the 30 min permeation carried out for GtG experiments.

Imaging and analysis. Samples were imaged using a Nikon LSM 710 equipped with a ×20 NA = 1.0 water immersion objective. Imaging settings of pinhole = 1.0 a.u., $\lambda = 488$ nm and z stack = 1.72 µm at Nyquist sampling were used to image hMSCs. The brightness and contrast of each channel was separately adjusted to better visualize the features prior to the generation of merged images both in ImageJ and IMARIS (Fig. 3c,g,h, Fig. 4a,d,e and Supplementary Fig. 6). Samples were visualized and segmented in IMARIS (Supplementary Fig. 8). For the separation of the nascent adhesions and 3DMAs, a 2D filter segmenting the paxillin channel with respect to ellipsoidal axis c with a threshold of 2 µm in non-scaled units, and sphericity with a threshold of 0.2, was used. Features satisfying >2 µm ellipsoidal axis c and <0.2 sphericity mostly qualified for 3DMAs; however, the segmentation was not perfect and sometimes required the manual addition and removal of features that did or did not resemble 3DMAs. Colocalizations (fibronectin–3DMA and paxillin–MT-MMP1) were also calculated in IMARIS using the 3D colocalization feature. As MT-MMP1 puncta were also observed outside of the cells (Fig. 4d), to quantify MT-MMP1 puncta per cell, the cell surface was first masked using a smoothed (1 µm in non-scaled units) segmentation of the paxillin channel, and MT-MMP1 puncta were quantified within the mask. The distance between paxillin and MT-MMP1 in colocalized puncta (Fig. 4h) were reported as the distance between the peak maxima of the Gaussian fits of paxillin and the MT-MMP1 line profiles measured in ImageJ.

Reporting summary
Further information on research design is available in the Nature Portfolio Reporting Summary linked to this article.

Data availability
The data used to prepare the figures, all displayed microscopy images and the raw images used to prepare these images are available at https://doi.org/10.25810/2eb5-8x48.

Code availability
The codes used for B-spline registration of the pre- and post-expansion images displayed in Fig. 2a are freely available at Koon et al.[52].

References

51. Thevenaz, P., Ruttimann, U. E. & Unser, M. A pyramid approach to subpixel registration based on intensity. *IEEE Trans. Image Process.* **7**, 27–41 (1998).
52. Koon, D.-J. B-spline grid, image and point based registration v.1.33.0.0 (MathWorks, 2011).
53. Vogler, T. O., Gadek, K. E., Cadwallader, A. B., Elston, T. L. & Olwin, B. B. Isolation, culture, functional assays, and immunofluorescence of myofiber-associated satellite cells. *Methods Mol. Biol.* **1460**, 141–162 (2016).
54. Yang, C., Tibbitt, M. W., Basta, L. & Anseth, K. S. Mechanical memory and dosing influence stem cell fate. *Nat. Mater.* **13**, 645–652 (2014).
55. Rao, V. V., Vu, M. K., Ma, H., Killaars, A. R. & Anseth, K. S. Rescuing mesenchymal stem cell regenerative properties on hydrogel substrates post serial expansion. *Bioeng. Transl. Med.* **4**, 51–60 (2019).
56. Dong, X., Al-Jumaily, A. & Escobar, I. C. Investigation of the use of a bio-derived solvent for non-solvent-induced phase separation (NIPS) fabrication of polysulfone membranes. *Membranes* **8**, 23 (2018).
57. Sim, S.-L. et al. Branched polyethylene glycol for protein precipitation. *Biotechnol. Bioeng.* **109**, 736–746 (2012).
58. Lu, S. & Anseth, K. S. Release behavior of high molecular weight solutes from poly(ethylene glycol)-based degradable networks. *Macromolecules* **33**, 2509–2515 (2000).
59. Cruise, G. M., Scharp, D. S. & Hubbell, J. A. Characterization of permeability and network structure of interfacially photopolymerized poly(ethylene glycol) diacrylate hydrogels. *Biomaterials* **19**, 1287–1294 (1998).
60. Merrill, E. W., Dennison, K. A. & Sung, C. Partitioning and diffusion of solutes in hydrogels of poly(ethylene oxide). *Biomaterials* **14**, 1117–1126 (1993).
61. Lustig, S. R. & Peppas, N. A. Solute diffusion in swollen membranes. IX. Scaling laws for solute diffusion in gels. *J. Appl. Polym. Sci.* **36**, 735–747 (1988).

Acknowledgements

Author contributions
K.A.G., B.B.O., E.S.B. and K.S.A. designed the experiments. K.A.G., T.-L.C., N.P.S. and V.V.R. carried out GtG experiments. K.A.G., L.J.M., N.P.S. and T.E.B. designed and prepared the PhotoExM formulations. T.-L.C., A.A.C. and J.S.S. carried out the expansion of muscle tissue sections and myofibres. K.A.G., N.P.S., C.Z. and C.-C.Y. carried out the non-rigid registration experiments. N.P.S. carried out the fluorophore photobleaching experiments. K.A.G. and K.S.A. wrote the paper. All authors contributed to the discussion of the data.

Competing interests

Additional information

Supplementary information The online version contains supplementary material available at https://doi.org/10.1038/s41563-023-01558-5.

Correspondence and requests for materials should be addressed to Kristi S. Anseth.

Peer review information *Nature Materials* thanks Kwanghun Chung and the other, anonymous, reviewer(s) for their contribution to the peer review of this work.

Reprints and permissions information is available at www.nature.com/reprints.

nature portfolio

Corresponding author(s): Kristi S. Anseth

Last updated by author(s): Feb 12, 2023

Reporting Summary

Nature Portfolio wishes to improve the reproducibility of the work that we publish. This form provides structure for consistency and transparency in reporting. For further information on Nature Portfolio policies, see our Editorial Policies and the Editorial Policy Checklist.

Statistics

For all statistical analyses, confirm that the following items are present in the figure legend, table legend, main text, or Methods section.

n/a	Confirmed	
☐	☒	The exact sample size (n) for each experimental group/condition, given as a discrete number and unit of measurement
☐	☒	A statement on whether measurements were taken from distinct samples or whether the same sample was measured repeatedly
☐	☒	The statistical test(s) used AND whether they are one- or two-sided *Only common tests should be described solely by name; describe more complex techniques in the Methods section.*
☒	☐	A description of all covariates tested
☒	☐	A description of any assumptions or corrections, such as tests of normality and adjustment for multiple comparisons
☐	☒	A full description of the statistical parameters including central tendency (e.g. means) or other basic estimates (e.g. regression coefficient) AND variation (e.g. standard deviation) or associated estimates of uncertainty (e.g. confidence intervals)
☐	☒	For null hypothesis testing, the test statistic (e.g. F, t, r) with confidence intervals, effect sizes, degrees of freedom and P value noted *Give P values as exact values whenever suitable.*
☒	☐	For Bayesian analysis, information on the choice of priors and Markov chain Monte Carlo settings
☒	☐	For hierarchical and complex designs, identification of the appropriate level for tests and full reporting of outcomes
☒	☐	Estimates of effect sizes (e.g. Cohen's d, Pearson's r), indicating how they were calculated

Our web collection on statistics for biologists contains articles on many of the points above.

Software and code

Policy information about availability of computer code

Data collection	Zeiss ZEN software 2012 SP5 FP3 (black) version 14.0.21.201 for imaging with Zeiss LSM710 Nikon Elements v5.30.05 for imaging with Nikon A1R TRIOS software v4.3.1.39215 for collection of rheological data with ARES R3 rheometer
Data analysis	Fiji (ImageJ) 2.1.0/1.53c for utilization of TurboReg plugin for image registration, quantification of resolution via tubulin imaging, determination of distance between sarcomeres, Matlab R2020b for B-spline registration of pre- and post-expansion tubulin immonolabeled samples. The code is available in citation 55. IMARIS v9.6.0 for 3d data analysis of hMSCs encapsulated in synthetic hydrogels as described in Section 4.5. GraphPad Prism 8 for statistical analysis (ANOVA tests, t-tests) and data plotting.

For manuscripts utilizing custom algorithms or software that are central to the research but not yet described in published literature, software must be made available to editors and reviewers. We strongly encourage code deposition in a community repository (e.g. GitHub). See the Nature Portfolio guidelines for submitting code & software for further information.

Data

Policy information about <u>availability of data</u>

All manuscripts must include a <u>data availability statement</u>. This statement should provide the following information, where applicable:
- Accession codes, unique identifiers, or web links for publicly available datasets
- A description of any restrictions on data availability
- For clinical datasets or third party data, please ensure that the statement adheres to our <u>policy</u>

The data used to prepare the Figures, all displayed microscopy images as well as raw images used to prepare these images are available at ....

Human research participants

Policy information about <u>studies involving human research participants and Sex and Gender in Research.</u>

Reporting on sex and gender	N/A
Population characteristics	N/A
Recruitment	N/A
Ethics oversight	N/A

Note that full information on the approval of the study protocol must also be provided in the manuscript.

Field-specific reporting

Please select the one below that is the best fit for your research. If you are not sure, read the appropriate sections before making your selection.

☒ Life sciences   ☐ Behavioural & social sciences   ☐ Ecological, evolutionary & environmental sciences

For a reference copy of the document with all sections, see nature.com/documents/nr-reporting-summary-flat.pdf

Life sciences study design

All studies must disclose on these points even when the disclosure is negative.

Sample size	No statistical methods to predetermine sample size were used. For the determination of expansion isotropy and resolution via tubulin full-width at half maxima (FWHM) measurements (Fig. 2a-d), previously published expansion microscopy paper was used as a precedent (Chen, F., Tillberg, P. W. & Boyden, E. S. Expansion microscopy. Science 347, 543–548 (2015)). For the determination of sarcomere lengths pre and post-expansion (Fig. 2f-g), comparable number of distance measurements were performed to that of tubulin FWHM measurements (N = 2 tissue sections both for pre- and post-expanded samples). The sample sizes for the post-expansion hMSC imaging in synthetic hydrogels (Fig 3 and 4) were primarily dictated by the available laser-scanning confocal microscope time, as each imaging took quite long: (~ 20 - 65 min. per cell). In these experiments, hMSCs were encapsulated in at least 2 independent hydrogels and a minimum of 19 cells were imaged per experimental condition. For the determination of PhotoExM hydrogel moduli and expansion factors, 3 hydrogels were used.
Data exclusions	No data were excluded from the analysis.
Replication	All experiments were replicated at at least twice, or at least two independent hydrogels were used for generation of the data during a single experiment. All replication attempts for the data presented in the manuscript was successful.
Randomization	For determinaton of PhotoExM resolution (Figure 2e), the samples immunolabeled with tubulin were randomly assigned and subjected to 4.58 or 6.5x expansion. Muscle tissue sections that were imaged before and after expansion were assigned randomly (Figure 2f). For all of the experiments summarized in Figure 3 and 4, hydrogel cultures that were fixed and D1, D3 and D7 were chosen randomly, and hydrogels that were immunolabeled for paxillin/fibronectin, collagen/integrin B1, laminin/integrin B1, paxillin/MT-MMP1 were chosen randomly.
Blinding	Blinding was not applied during the experiments, as low throughput imaging, which required locating the post-expanded samples by the investigator rendered blinding unfeasible for most of this study especially for the experiments demonstrated in Figure 3 and 4. However, imaging was performed in the random locations of the hydrogel, and the data were obtained via semi-automated image analysis to minimize the effect of unblinding.

Reporting for specific materials, systems and methods

We require information from authors about some types of materials, experimental systems and methods used in many studies. Here, indicate whether each material, system or method listed is relevant to your study. If you are not sure if a list item applies to your research, read the appropriate section before selecting a response.

Materials & experimental systems

n/a	Involved in the study
☐	☒ Antibodies
☐	☒ Eukaryotic cell lines
☒	☐ Palaeontology and archaeology
☐	☒ Animals and other organisms
☒	☐ Clinical data
☒	☐ Dual use research of concern

Methods

n/a	Involved in the study
☒	☐ ChIP-seq
☒	☐ Flow cytometry
☒	☐ MRI-based neuroimaging

Antibodies

Antibodies used	anti-alpha-tubulin (1:250, Abcam ab7291, clone DM1A), anti-alpha-actinin (1:250, Sigma Aldrich A7811, clone EA-53, lot# 0000120830), anti-fibronectin (1:250, Abcam ab6328, clone IST-9, lot# GR3356983-1), anti-paxillin (1:150, Abcam ab32084, clone Y113, lot# GR215998-32), anti-collagen I (1:200, Abcam ab34710), anti-laminin (1:200, Abcam ab11575, lot# GR3268366-7), anti-MT-MMP1 (1:100, Santa Cruz Biotechnology sc-373908, clone C-9, lot# L1817), anti-CD29 (1:250, BD bioscience 553715, clone 9EG7), anti-pax7 (1:250, developmental studies hybridoma bank, RRID:AB_528428 lot# 4), anti-laminin (1:63, Sigma Aldrich L9393), anti-dystrophin (1:63, Abcam ab15277), donkey anti-mouse IgG Alexa Fluor Plus 488 (1:250, ThermoFisher A32766, lot# WF319853), goat anti-rabbit IgG Alexa Fluor Plus 594 (1:250, ThermoFisher A32740), goat anti-rat IgG Alexa Fluor 488 (1:250, ThermoFisher A-11006), goat anti-rabbit IgG Alexa Fluor 546 (1:250, ThermoFisher A-11035)
Validation	mouse anti-alpha-tubulin, species reactivity for mouse tubulin indicated on manufacturer's website (ref. Sci Rep. 2020 doi: 10.1038/s41598-020-71167-8); mouse anti-alpha-actinin, species reactivity for mouse skeletal muscle actinin indicated on manufacturer's website (ref. Anat Rec (Hoboken). 2014 doi: 10.1002/ar.22981); mouse anti-fibronectin, species reactivity for human fibronectin indicated on manufacturer's website (ref. Stem Cell Res Ther. 2019 doi: 10.1186/s13287-019-1431-6); rabbit anti-paxillin, species reactivity for human paxillin alpha, beta and gamma isoforms indicated on manufacturer's website (ref. Integr Biol (Camb). 2016 doi: 10.1039/c6ib00076b); rabbit anti-collagen I, species reactivity for human collagen type I indicated on manufacturer's website (ref. Biotechnol Bioeng. 2019 doi: 10.1002/bit.26957); rabbit anti-laminin, species reactivity for human laminin indicated on manufacturer's website (ref. Front Cell Dev Biol. 2020 doi: 10.3389/fcell.2020.555378); mouse anti-MT-MMP1, species reactivity for human MT-MMP-1 indicated on manufacturer's website (ref. Adv Healthc Mater. 2022 doi: 10.1002/adhm.202101592); mouse anti-CD29, species reactivity for human integrin beta 1 indicated on the original publication of this 9EG7 antibody (ref. PNAS, 1993 doi: 10.1073/pnas.90.19.905); mouse anti-pax7, species reactivity for nuclei of mouse skeletal muscle satellite cells indicated on manufacturer's website (ref. Sci Adv. 2021 doi: 10.1126/sciadv.abe4501); rabbit anti-laminin, species reactivity for both human and animal laminin indicated on manufacturer's website (ref. Sci Adv. 2021 doi: 10.1126/sciadv.abe4501); rabbit anti-dystrophin, validated for mouse skeletal muscle satellite cells on manufacturer's data sheet (ref. Cell Stem Cell. 2022 doi: 10.1016/j.stem.2021.11.003)

Eukaryotic cell lines

Policy information about cell lines and Sex and Gender in Research

Cell line source(s)	hMSCs were isolated from human bone marrow aspirate purchased from Lonza, and the bone marrow was isolated from an 18 year old black female. C2C12 (myoblast) cell line was obtained from ATCC, Cat# CRL-1772.
Authentication	Flow cytometry analysis was used to determine that 95% of the hMSCs were positive for CD73, CD90, and CD105. hMSCs also possessed spindle like morphology and were able to differentiated into osteoblasts and adipocytes. The C2C12 cell line authentication was performed by ATCC according to the information on the manufacturer's webpage. Briefly, the C2C12 cell line formed contractile myotubes and produced characteristic muscle proteins and furthermore, C2C12 cells lines were characteristically immunoreactive towards Pax7 and MyoD.
Mycoplasma contamination	Both hMSCs and C2C12 were negative for mycoplasma contamination in 2020.
Commonly misidentified lines (See ICLAC register)	No commonly misidentified cell lines were used.

Animals and other research organisms

Policy information about studies involving animals; ARRIVE guidelines recommended for reporting animal research, and Sex and Gender in Research

Laboratory animals	C57BL/6J mice, 6 month old, male. The housing condition of mice: Temperature of 69°F-75°F with 10% humidity and 12-hour light/12-hour dark cycles.
Wild animals	This study did not involve samples collected from the field.
Reporting on sex	In this study, only male mice were used. Since we were using sacromeres of mouse skeletal muscle to validate the application of

Reporting on sex	PhotoExM on tissue sections and the expansion factor rather than conducting a biological study, sex was not considered as a significant factor in this study.
Field-collected samples	This study did not involve samples collected from the field.
Ethics oversight	Mice were bred and housed according to National Institutes of Health (NIH) guidelines for the ethical treatment of animals in a pathogen-free facility at the University of Colorado at Boulder. The University of Colorado Institutional Animal Care and Use Committee (IACUC) approved all animal protocols and procedures.

Note that full information on the approval of the study protocol must also be provided in the manuscript.